Chinese Physics Letters

LETTER

Anharmonicity Driven by Vacancy Ordering Unlocks High-Performance Thermoelectric Conversion in Defective Chalcopyrites II-III$_2$-VI$_4$

Cite as: Hui Zhang *et al*. 2026 *Chin. Phys. Lett.* **43** 080803

DOI CSTR

Recommended Articles

Machine-Learning Accelerated Discovery of High-Performance Thermal Switch in Two-dimensional Materials Considering High-order Anharmonicity
Jie Sun, Han Meng, Rulei Guo, Long Cheng, Yiheng Shen, and Xiaoliang Zhang
Chin. Phys. Lett. **42**, 110701 (2025)

Synergistic Optimization of Electronic Structure and Defects via Light Zn-Doping for High Performance n-Type $Bi_2(Te, Se)_3$ Thermoelectrics in Cooling and Power Generation
Jiayi Peng *et al*.
Chin. Phys. Lett. **43**, 030803 (2026)

Influence of High-Pressure Induced Lattice Dislocations and Distortions on Thermoelectric Performance of Pristine SnTe
Bowen Zheng, Tao Chen, Hairui Sun, Manman Yang, Bingchao Yang, Xin Chen, Yongsheng Zhang, and Xiaobing Liu
Chin. Phys. Lett. **41**, (2024)

Anharmonic Phonon Dynamics and the Origin of Ultralow Lattice Thermal Conductivity in $CuBiI_4$: Implications for Thermoelectric Applications
Feng Xiao, Qing-Yu Xie, Ru Yu, Junrong Zhang, and Bao-Tian Wang
Chin. Phys. Lett. **42**, 120702 (2025)

A Comparative Study on the Thermoelectric Performance of Layered β- and ε-GaSe
Wenyan Jiao, Hongmei Yuan, Shihao Han, Yufeng Luo, Haibin Cao, and Huijun Liu
Chin. Phys. Lett. **42**, 080603 (2025)

A series journal of Chinese Physical Society distributed by IOP Publishing

Chinese Physics Letters

Chin. Phys. Lett. **43** 080803 (2026)

LETTER

DOI: 10.1088/0256-307X/43/8/080803
CSTR: 32039.14.0256-307X.43.8.080803

Anharmonicity Driven by Vacancy Ordering Unlocks High-Performance Thermoelectric Conversion in Defective Chalcopyrites II-III$_2$-VI$_4$

Hui Zhang[1,†], Jincheng Yue[2,3,1,†,*], Jiongzhi Zheng[4,5], Ning Wang[1], Wenling Ren[6], Shuyao Lin[7,8], Chen Shen[9,10], Hao Gao[3], Yanhui Liu[1,*], Yue-Wen Fang[2,11,*], and Tian Cui[1,*]

[1]Institute of High-Pressure Physics, School of Physical Science and Technology, Ningbo University, Ningbo 315211, China
[2]Centro de Física de Materiales (CFM-MPC), CSIC-UPV/EHU, Manuel de Lardizabal Pasealekua 5, 20018 Donostia/San Sebastián, Spain
[3]Fisika Aplikatua Saila, Gipuzkoako Ingeniaritza Eskola, University of the Basque Country (UPV/EHU), Europa Plaza 1, 20018 Donostia/San Sebastián, Spain
[4]Energy Technologies Area, Lawrence Berkeley National Laboratory, Berkeley, CA 94720, United States of America
[5]Thayer School of Engineering, Dartmouth College, Hanover, NH 03755, United States of America
[6]Institute of Materials Science, Technical University of Darmstadt, Alarich-Weiss-Strasse 2, Darmstadt, 64287, Germany
[7]Technische Universität Wien, Institute of Materials Science and Technology, Vienna, A-1060, Austria
[8]Linköping University, Department of Physics, Chemistry, and Biology (IFM), Linköping, SE-58183, Sweden
[9]Suzhou Laboratory, Suzhou 215000, China
[10]Gusu Laboratory of Materials, Suzhou 215031, China
[11]Instituto de Nanociencia y Materiales de Aragón (INMA), CSIC-Universidad de Zaragoza, Zaragoza, 50009, Spain

[†]These authors contributed equally to this work.
[*]Corresponding authors. Email: jyue001@ikasle.ehu.eus; liuyanhui@nbu.edu.cn; yuewen.fang@csic.es; cuitian@nbu.edu.cn

Defective chalcopyrites have recently emerged as promising thermoelectric materials because their ordered intrinsic vacancies can profoundly reshape both lattice dynamics and electronic structure. Here, we present a comprehensive theoretical investigation of the lattice thermal and carrier transport properties of II-III$_2$-VI$_4$ defective chalcopyrites by combining first-principles calculations with machine-learning interatomic potentials. We show that vacancy ordering enhances lattice distortion, leading to strong anharmonicity and metavalent bonding. The interplay of soft low-frequency phonons, strongly negative Grüneisen parameters, and a substantially enlarged four-phonon-scattering phase space strongly regulates heat transport, yielding an ultralow lattice thermal conductivity. Meanwhile, systematic anion substitution at the VI-site provides an effective route to tune the electronic structure: reduced anion electronegativity weakens metal-anion hybridization, shifts anion p states upward, narrows the band gap, and thereby improves electrical transport. Benefiting from this synergy between vacancy-induced phonon suppression and anion-regulated electronic optimization, CdGa$_2$Te$_4$ exhibits an ultralow lattice thermal conductivity of 0.19 W·m^{-1}·K^{-1} and a high room-temperature *ZT* of 0.689. This work not only predicts defective chalcopyrites as a promising platform for high-performance thermoelectrics but also provides a practical design strategy by integrating vacancy ordering, higher-order phonon scattering, and anion-dependent band engineering.

Introduction

Diamond-like compounds have emerged as a research hotspot in the field of thermoelectric materials due to their tetrahedrally coordinated crystal structures that can be traced back to binary zinc blende or wurtzite frameworks [1−7]. Among them, representative systems with chalcopyrite (I-III-VI$_2$) have been widely investigated as well-known lattice-distorted thermoelectric materials [8−13]. Their inherent lattice distortion induces strong lattice anharmonicity [14,15] and gives rise to ultralow lattice thermal conductivity (κ_L) that is a crucial foundation for high-performance thermoelectric materials [16,17]. In addition, the electronic band structures are highly tunable in chalcopyrite compounds [18,19]. For instance, substituting anionic components can effectively modulate the band gap, thereby optimizing electronic transport properties [9,19]. To fully exploit the potential of these materials for applications, researchers have conducted extensive efforts in thermoelectric performance optimization in recent years through strategies such as element doping [20,21] and external pressure [10,18].

Although external stimuli can effectively improve thermoelectric performance, exploring compounds with intrinsic lattice distortion characteristics is crucial for fundamentally optimizing material properties [22−24]. Xie *et al.* [25] recently demonstrated that the large tetrahedral distortion parameter η ($\eta = |2 - c/a|$) in silver-based chalcopyrites drives their intrinsic low lattice thermal conductivity. In-depth analysis reveals that this distortion induces strong lattice anharmonicity by breaking local tetrahedral symmetry, thereby significantly enhancing phonon scattering and ultimately suppressing the lattice thermal conductivity. Compared to traditional strategies that rely on external doping to introduce point defects for phonon scattering, intrinsic distortion achieves effective suppression of lattice thermal transport through the inherent characteristics of the crystal structure [26], offering new possibilities for the development of a new generation of high-performance thermoelectric materials.

Defective chalcopyrites (II-III$_2$-VI$_4$) typically crystallize an ordered vacancy structure derived from the evolution of the chalcopyrite structure, achieved by doubling the original formula unit and removing one group-I atom, thereby creating vacancies at the original group-I atomic sites [25]. The chalcopyrite structure ($I\bar{4}2d$, No. 122) itself can be traced back to the ternary diamondoid compounds, as shown in Fig. 1(a). It essentially comprises a double zinc blende cell ($F\bar{4}3m$, No. 216) stacked along the *c*-axis, where monovalent and trivalent cations replace the divalent cation. In zinc blende, all tetrahedral

Received 12 May 2026; accepted 20 July 2026; published 28 August 2026
© 2026 Chinese Physical Society and IOP Publishing Ltd. All rights, including for text and data mining, AI training, and similar technologies, are reserved.

Check for updates

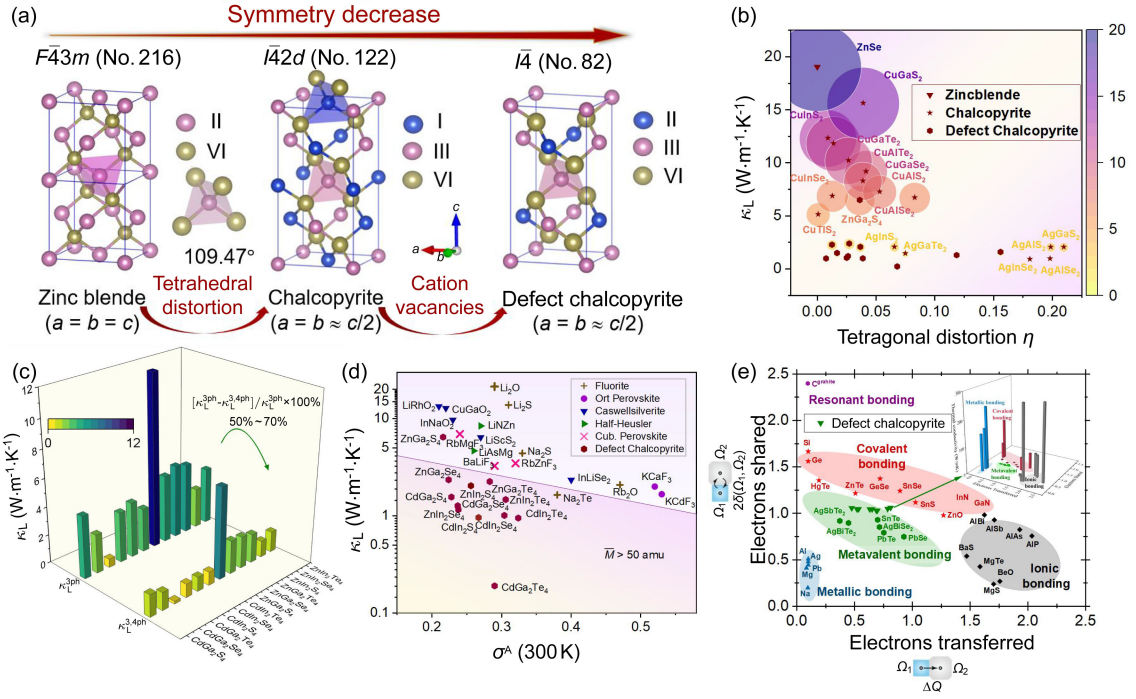

Fig. 1. (a) The crystal structures of zinc blende, chalcopyrite, and defective chalcopyrites. (b) The relationship between the η and the κ_L of different compounds. The related data are available in Ref. [25]. (c) The κ_L evaluated by including both $\kappa_L^{3,4ph}$ and κ_L^{3ph}. The color scale represents the κ_L. (d) The κ_L as a function of the lattice anharmonicity index σ^A at 300 K. The data for other compounds are given in Ref. [27]. (e) The quantum mechanics diagram of bonding in solids. The data for other compounds can be found in Ref. [28].

coordination units are formed with perfect tetrahedral symmetry, and its structure can be characterized by a cubic lattice ($a = b = c$) and a unity tetragonal distortion ($\eta = 0$). While the tetrahedral framework is preserved, it results in a tetragonal distortion characterized by $\eta \neq 0$ and a deviation of bond angles from the ideal value (109.47°), collectively manifesting the initial breaking of tetrahedral symmetry. The further introduction of vacancies induces a second symmetry-lowering to $I\bar{4}$ (No. 82), thereby intensifying the lattice distortion. As a result, the symmetry is reduced from $F\bar{4}3m$ to $I\bar{4}2d$, and then further decreases to $I\bar{4}$. Low-symmetry thermoelectric materials typically feature low κ_L due to structure complexity. Therefore, defective chalcopyrites also accommodate ultralow lattice thermal conductivity, with a magnitude comparable to the low κ_L reported in other thermoelectric materials [29,30]. This remarkable property renders it promising for thermoelectric applications, driving us to conduct systematic research on defective chalcopyrites.

In this work, we carry out a comprehensive investigation of the thermoelectric properties of defective chalcopyrites II-III$_2$-VI$_4$ by combining first-principles calculations with machine-learning interatomic potentials. We show that intrinsic vacancy ordering is not merely a crystallographic feature, but a key structural origin of the strong lattice anharmonicity in these materials. The vacancy-induced symmetry lowering and local lattice distortion foster metavalent bonding (MVB) and soften low-frequency phonons, which collectively enhance higher-order phonon interactions. This ultimately renders four-phonon (4ph) scattering a key factor for suppressing lattice thermal conductivity. In parallel, we reveal a clear anion-dependent electronic trend: as the electronegativity of the VI-site anion decreases, weakened orbital hybridization and the upward shift of anion p states cooperatively narrow the band gap and improve electrical transport. As a result, $CdGa_2Te_4$ emerges as the best-performing member of this family, combining an ultralow lattice thermal conductivity of 0.19 W·m^{-1}·K^{-1} with a room-temperature ZT of 0.689. These findings clarify the coupled roles of vacancy ordering and anion engineering in regulating phonon and carrier transport, and provide a viable design strategy for high-performance chalcopyrite-based thermoelectric materials.

Results and Discussion

Before discussing the thermoelectric properties, we examined the mechanical and thermodynamic stability of the defective chalcopyrites. Convex hull analysis based on the Open Quantum Materials Database (OQMD) [31] in Fig. S8 of the Supplementary Materials (SM) confirms that the investigated compounds are thermodynamically stable. The results confirm that the investigated structures are stable, thereby providing a reliable basis for the subsequent thermoelectric analysis. The detailed stability criteria and calculated results are summarized in the SM. As mentioned, the distortion parameter η not only critically influences κ_L but also serves as a fundamental indicator of lattice anharmonicity. Generally, a larger η indicates the greater deviation of the chalcopyrite lattice from the ideal diamond structure [19]. Such a structural distortion directly reflects an increase in lattice anharmonicity, which in turn effectively suppresses lattice thermal conductivity. As shown in Fig. 1(b), a relatively high κ_L is observed in the ideal cubic zinc blende structure ZnSe ($\eta = 0$). As the lattice undergoes tetragonal distortion to chalcopyrite, the κ_L significantly decreases. This trend clearly demonstrates that κ_L is strongly suppressed as η increases because of the enhanced lattice anharmonicity. Moreover, defective chalcopyrites possess lower-symmetry space groups and have more strongly distorted frameworks than chalcopyrite due to the presence of intrinsic cation vacancies. As expected, defective chalcopyrites promote intrinsically low lattice thermal conductivity, underscoring their potential as thermoelectric materials.

Chalcopyrites inherently feature pronounced phonon scattering driven by tetrahedral distortion, making higher-order processes indispensable for an accurate description [10,16]. Indeed, in $CuInTe_2$, the incorporation of 4ph scattering results in a substantial reduction in κ_L by 54.6% at 800 K [32]. By contrast, defective chalcopyrites experience even stronger anharmonic scattering, arising from the cooperative effects of tetrahedral distortion and vacancy-induced local lattice perturbations. Figure 1(c) shows the κ_L [including three-phonon (3ph) and 4ph scattering] as a function of temperature for defective chalcopyrites. Our results reveal that the inclusion of 4ph scattering leads to a 50%–70% reduction in lattice thermal conductivity in defective chalcopyrites at 300 K. Specifically, for $CdGa_2Te_4$, the inclusion of

4ph scattering at 300 K reduces κ_L from 0.61 $W\cdot m^{-1}\cdot K^{-1}$ (with only 3ph scattering) to 0.19 $W\cdot m^{-1}\cdot K^{-1}$, corresponding to a reduction of 68%. In addition, when only 3ph scattering is considered, the calculated κ_L of $ZnIn_2Te_4$ and $CdIn_2Te_4$ are 4.05 $W\cdot m^{-1}\cdot K^{-1}$ and 3.12 $W\cdot m^{-1}\cdot K^{-1}$ at 300 K, respectively. These values are substantially higher than the experimentally reported κ_L of 2.1 $W\cdot m^{-1}\cdot K^{-1}$ for $ZnIn_2Te_4$ and 1.2 $W\cdot m^{-1}\cdot K^{-1}$ for $CdIn_2Te_4$ [33], indicating that a description based solely on third-order anharmonicity overestimates κ_L. Upon explicitly incorporating 4ph scattering processes, the predicted κ_L are significantly reduced to 1.47 $W\cdot m^{-1}\cdot K^{-1}$ and 0.95 $W\cdot m^{-1}\cdot K^{-1}$ for $ZnIn_2Te_4$ and $CdIn_2Te_4$, respectively, yielding much closer agreement with experiment. Notably, the remaining small deviation between our calculated and experimental values could also be influenced by factors such as sample quality and measurement accuracy, which are not accounted for in our ideal single-crystal model. These results suggest that the cooperative effects of tetrahedral distortion and cation vacancies give rise to strong 4ph scattering processes, whose contributions are essential for a reliable quantitative evaluation of κ_L in defective chalcopyrites.

To quantify the strength of anharmonic effects in a material, we calculate the anharmonicity index $\sigma^A(T)$, defined as [34]:

$$\sigma^A(T) \equiv \frac{\sigma[F^A]_T}{\sigma[F]_T} = \sqrt{\frac{\sum_{I,\alpha}\left\langle \left(F^A_{I,\alpha}\right)^2\right\rangle_T}{\sum_{I,\alpha}\left\langle \left(F_{I,\alpha}\right)^2\right\rangle_T}}. \quad (1)$$

A value of $\sigma^A(T) > 0.2$ indicates that anharmonic interactions become comparable in magnitude to harmonic interactions [34]. As shown in Fig. 1(d), $\sigma^A(T = 300\ K)$ values for defective chalcopyrites primarily lie in the range of 0.22–0.33. Among them, $ZnGa_2S_4$ exhibits the smallest σ^A(300 K) and the largest κ_L (6.46 $W\cdot m^{-1}\cdot K^{-1}$), whereas $CdIn_2Te_4$ shows the largest σ^A(300 K) and a much lower κ_L (0.95 $W\cdot m^{-1}\cdot K^{-1}$). Extending the analysis to a broader range of materials with σ^A(300 K) values from 0.2 to 0.6, including simple binary compounds, perovskites, and chalcopyrite-type systems, most materials are found to possess κ_L below 10 $W\cdot m^{-1}\cdot K^{-1}$. Notably, defective chalcopyrites tend to show even lower κ_L than other materials at comparable levels of anharmonicity. This behavior can be largely attributed to their relatively high mean atomic mass ($\overline{M}$) and the presence of intrinsic vacancies. Most of the defective chalcopyrites have an $\overline{M}$ greater than 50 amu (except $ZnGa_2S_4$ at 47.58 amu) [35], while materials with higher κ_L typically consist of lighter atoms. These results suggest that the ultralow κ_L in defective chalcopyrites arises from the synergistic effects of strong lattice anharmonicity, heavy atomic masses, and vacancy-induced phonon scattering.

On the other hand, intrinsic low lattice thermal conductivity is closely linked to the nature of its atomic bonding. Figure 1(e) summarizes the charge transfer and the number of shared electron pairs based on atomic net charge Q_i (reflecting electron transfer) and delocalization index $\delta(\Omega_i,\Omega_j)$ (quantifying covalent interactions between atoms) [36]. These two descriptors clearly delineate bonding regimes associated with ionic, covalent, metallic, and MVB. Notably, defective chalcopyrites lie within the central green region, which corresponds to the MVB domain characterized by distinct transitional bonding behavior. Its bonding is characterized by approximately 0.8e of shared electrons per bond, which is intermediate between conventional covalent bonding with highly localized electron sharing and metallic bonding with strongly delocalized electrons. Such unconventional bonding is considered the origin of its exceptionally low lattice thermal conductivity [36,37], as highlighted in the inset of Fig. 1(e). Detailed data for defective chalcopyrites are provided in Table S2 in the SM. Microscopically, this behavior arises from strong bond-induced lattice anharmonicity, manifested as a large Grüneisen parameter [28]. Previous studies have shown that the intrinsically distorted tetrahedral configuration in silver-based chalcopyrite materials $AgXY_2$ promotes the formation of MVB [38], leading to the softening of low-frequency optical phonons and the suppression of κ_L. As a result, cation vacancies in defective chalcopyrites induce lattice distortion that promotes MVB and thereby introduces strong lattice anharmonicity, which ultimately leads to its extremely low lattice thermal conductivity.

For a comprehensive investigation of lattice thermal transport, $CdGa_2Te_4$ and $ZnGa_2S_4$ with the lowest and highest κ_L were selected for comparison. As shown in Fig. 2(a), the calculated phonon dispersions of $CdGa_2Te_4$ and $ZnGa_2S_4$ do not show any imaginary modes, confirming their dynamical stability. The two compounds nevertheless differ markedly in the low-frequency region. The $ZnGa_2S_4$ possesses a higher-lying lowest acoustic branch across the Brillouin zone, whereas softer acoustic phonons characterize $CdGa_2Te_4$. To quantify the long-wavelength lattice vibrations, we linearly fitted the lowest acoustic branch along the Γ–M direction. The fitted slope for $ZnGa_2S_4$ is 2.04 THz·Å, which is substantially larger than the value of 0.61 THz·Å obtained for $CdGa_2Te_4$, implying a higher acoustic phonon group velocity in $ZnGa_2S_4$. This trend is mainly associated with the larger average atomic mass of $CdGa_2Te_4$, which lowers the vibrational frequencies and is expected to suppress the lattice thermal conductivity.

Consistent with Fig. 2(a), the phonon density of states (DOS) in Fig. 2(b) shows that $CdGa_2Te_4$ is characterized by pronounced peaks dominated by Cd- and Te-derived vibrations, reflecting the dominant role of heavy atoms in the low-frequency modes. In contrast, $ZnGa_2S_4$ displays broader DOS features arising from the collective contributions of Zn, Ga, and S. Furthermore, we plotted the Grüneisen parameter for $CdGa_2Te_4$ and $ZnGa_2S_4$ in Fig. 2(c). Within the 0–2 THz range, the Grüneisen parameter of $ZnGa_2S_4$ stays close to zero and only reaches a mildly negative value of about −1.6, showing no pronounced peak and thus indicating relatively weak anharmonicity. On the other hand, a strongly negative Grüneisen parameter appears in $CdGa_2Te_4$ over the same frequency window, with a pronounced minimum of around −10. This large negative value suggests that the presence of heavy atoms is closely linked to strong lattice anharmonicity, which in turn promotes enhanced higher-order phonon–phonon scattering.

Next, the influences of third- and fourth-order anharmonicity on phonon lifetime and scattering rates are investigated at 300 K. As seen from Fig. 2(d), $CdGa_2Te_4$ displays significantly shorter $\tau_{3,4ph}$ than $ZnGa_2S_4$, particularly in the low-frequency region where $\tau_{3,4ph}$ is reduced by more than one order of magnitude. Such a difference in phonon lifetime is mainly attributed to the stronger lattice anharmonicity in $CdGa_2Te_4$, which enhances the scattering rates. The reduced group velocity in $CdGa_2Te_4$ does not affect the lifetime itself, but it indicates slower phonon propagation and thus less efficient heat transport, further suppressing the lattice thermal conductivity.

Within the frequency interval where the Grüneisen parameter shows pronounced negative peaks, the low-frequency modes that are mainly associated with the heavy Cd and Te atoms experience stronger anharmonic interactions, which further shorten the phonon lifetime. In addition, separating the 3ph and 4ph contributions to the scattering rates reveals that, in the low-frequency range of $CdGa_2Te_4$, the 4ph scattering rates are nearly an order of magnitude higher than those from 3ph processes, indicating their significant role in suppressing the $\tau_{3,4ph}$. By contrast, $ZnGa_2S_4$ shows similar magnitudes of 3ph and 4ph scattering rates in the same low-frequency region, implying comparable contributions from the two scattering processes. For both materials, 3ph scattering rates become dominant above around 3.5 THz, particularly in $ZnGa_2S_4$. Taken together, the sharp reduction of phonon lifetime in $CdGa_2Te_4$ can be mainly attributed to the strongly enhanced higher-order scattering. In combination with its lower phonon group velocity, this leads to a stronger suppression of lattice thermal transport in $CdGa_2Te_4$ than in $ZnGa_2S_4$.

To further elucidate the significant role of 4ph processes, the spectral and cumulative κ_L shown in Fig. 2(e) are calculated with and without 4ph scattering for comparison. For $CdGa_2Te_4$, the reduction of κ_L caused by 4ph scattering is mainly located in 0–1.5 THz. The spectral heat-carrying contributions associated with 4ph and 3ph scattering show little overlap in this interval, which indicates that low-frequency heat transport is largely controlled by 4ph scattering. By contrast, although 4ph scattering in $ZnGa_2S_4$ also decreases κ_L to some extent especially in 1–3 THz, its overall impact is weaker than in

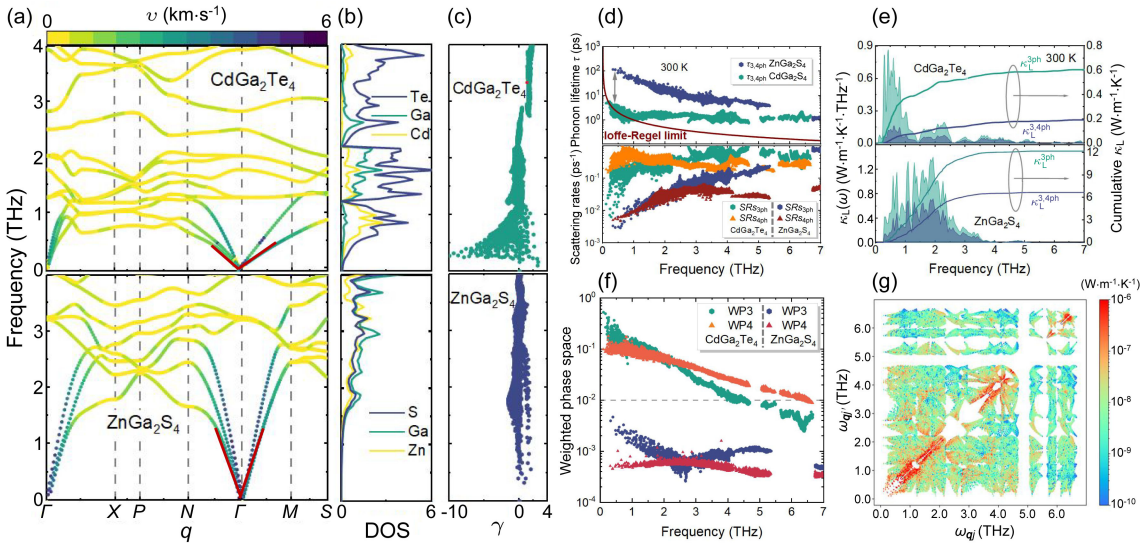

Fig. 2. (a) Phonon dispersions in 0–4 THz. (b) The phonon DOS. (c) The Grüneisen parameters γ against the phonon frequency. (d) Phonon lifetimes $\tau_{3,4ph}$ including 3ph and 4ph scattering processes, as well as the scattering rates of 3ph (SRs_{3ph}) and 4ph (SRs_{4ph}), calculated at 300 K for $CdGa_2Te_4$ and $ZnGa_2S_4$. (e) The spectral/cumulative lattice thermal conductivity at 300 K. (f) WP3 and WP4 at 300 K. (g) The calculated $\kappa_C(\omega_{qj},\omega_{qj'})$ for $CdGa_2Te_4$ at 300 K.

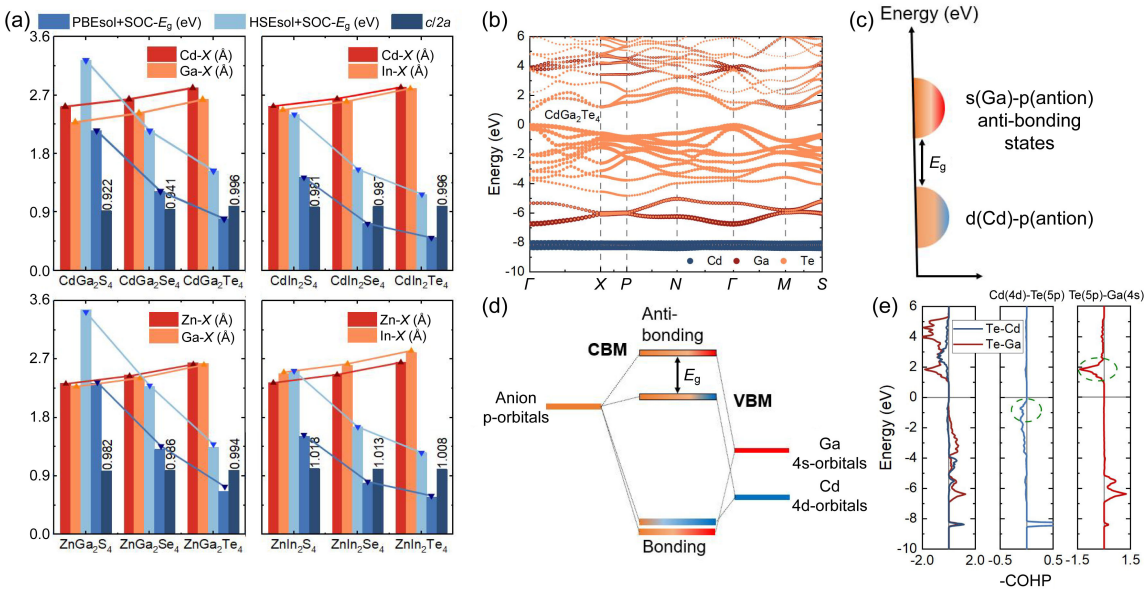

Fig. 3. (a) Calculation results of bond lengths, structural parameter $c/2a$, and electronic band gaps with PBEsol+SOC (spin–orbit coupling) and HSEsol+SOC functionals for defective chalcopyrites. Detailed band gap data are provided in the SM. (b) The atom-projected band structure of $CdGa_2Te_4$. (c) Schematic DOS with Cd-anion antibonding as the valence band edge and Ga-anion antibonding states as the conduction band edge. (d) Schematic molecular-orbital diagram. (e) Crystal orbital Hamilton population (COHP).

$CdGa_2Te_4$. Further insight into this contrast is obtained from the weighted phase space in Fig. 2(f). The 4ph weighted phase space (WP4) of $CdGa_2Te_4$ is about two orders of magnitude larger than that of $ZnGa_2S_4$, which points to a larger number of available 4ph scattering processes. Remarkably, WP4 is comparable to the 3ph weighted phase space (WP3) in $CdGa_2Te_4$, so that 4ph and 3ph scattering share similar phase-space and higher-order processes can occur with high probability [39]. In $ZnGa_2S_4$, however, WP3 remains dominant in 0–2 THz. Only in 2–3 THz does WP4 become comparable to WP3, a trend that is consistent with the phonon spectrum of $ZnGa_2S_4$. Hence, in $CdGa_2Te_4$, the substantial WP4 and the pronounced intrinsic anharmonicity work together, where the former provides scattering processes, and the latter strengthens phonon–phonon coupling. Together, they markedly enhance the scattering rate, thereby severely suppressing the lattice thermal conductivity. To examine whether the 4ph scattering necessarily involves a wave-tunneling phonon transport mechanism [40,41], we calculated the coherent lattice thermal conductivity of $CdGa_2Te_4$. As shown in Fig. 2(g) and Fig. S9 of the SM, the results indicate that quasi-degenerate phonon modes ($\omega_{qj} \approx \omega_{qj'}$) provide the main contribution to the coherent conductivity [42]. The maximum value of this contribution is only 10^{-6} $W{\cdot}m^{-1}{\cdot}K^{-1}$, negligible compared with the total lattice thermal conductivity.

As manifested in Fig. 3(a), there is a strong correlation between bond length, tetragonal distortion, and the band gap E_g in defective chalcopyrites. For the $CdGa_2X_4$ (X = S, Se, Te), both Cd-X and Ga-X bond lengths increase monotonically as the electronegativity of the VI-site anion decreases with the cation fixed, accompanied by an increase in $c/2a$ from 0.922 to 0.996, approaching the limit of $c/2a = 1$. In parallel, the calculated E_g decreases markedly with increasing bond length, and the same monotonic trend is also observed in the Zn-based counterparts. Since Perdew–Burke–Ernzerhof revised for solids (PBEsol) tends to underestimate E_g, Heyd–Scuseria–Ernzerhof revised for solids (HSEsol) results are included to provide a consistent comparison of the gap evolution. The above trend originates from the

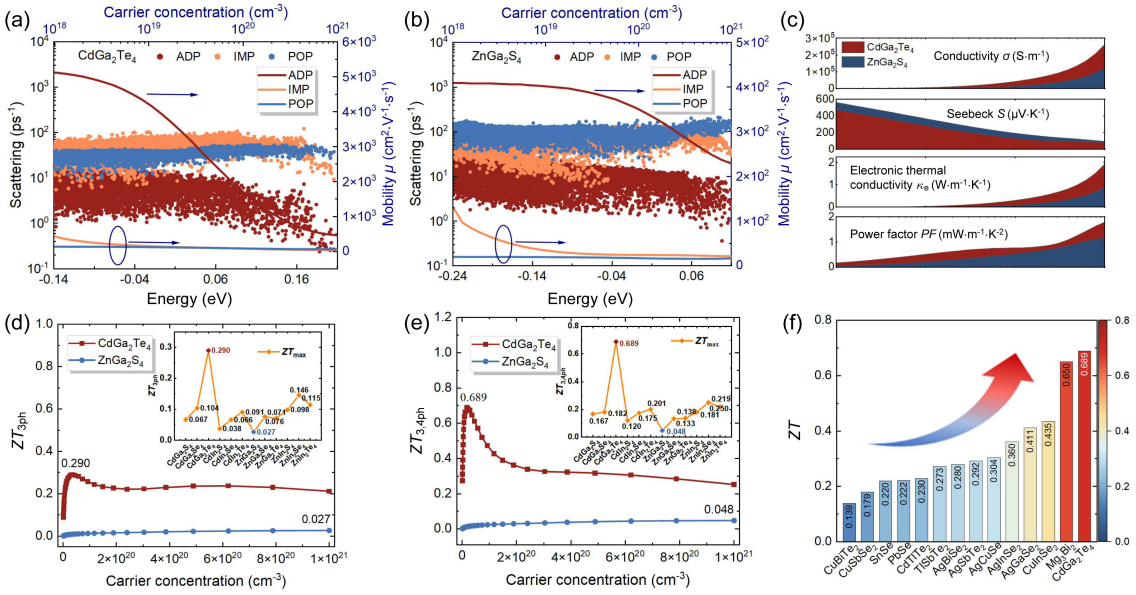

Fig. 4. The scattering rates of ADP, IMP, and POP mechanisms for (a) $CdGa_2Te_4$ and (b) $ZnGa_2S_4$ at 300 K and a carrier concentration of 10^{21} cm^{-3}, and the corresponding carrier mobilities as functions of carrier concentration. (c) The calculated results of σ, S, κ_e, and PF of $CdGa_2Te_4$ and $ZnGa_2S_4$ with varying carrier concentrations. The variation of (d) ZT_{3ph} and (e) $ZT_{3,4ph}$ of $CdGa_2Te_4$ and $ZnGa_2S_4$ with carrier concentration considering. (f) Comparison of ZT between $CdGa_2Te_4$ and other typical thermoelectric compounds at 300 K, where the specific compounds corresponding to the labels are detailed in Refs. [43–49].

differences in the intrinsic properties of the anions. With decreasing electronegativity of the VI-site anion and the cation fixed, the larger atomic radius weakens the cation-anion bonding, resulting in increased bond lengths and a gradual diminishment of tetragonal distortion. These two factors collectively influence the electronic band structure, resulting in a monotonic decrease in the E_g with increasing anion atomic number.

The band structure, atom-projected DOS, and bonding analysis for $CdGa_2Te_4$ were calculated to reveal the microscopic origin of the band gap reduction, as shown in Figs. 3(b)–3(e). The band structure indicates a direct gap at Γ, with pronounced band degeneracy at the valence band maximum (VBM). As the electronegativity of the VI-site anion decreases with the cation fixed, the energy separation at the Γ point between the valence bands near VBM gradually increases, while the band curvature near the Fermi level increases correspondingly (see SM Figs. S10–S13 for details). This increased curvature results in relatively steep band regions. The projected DOS shows that the VBM is dominated by Te-5p states, and the conduction band minimum (CBM) mainly originates from Ga-s states with appreciable Te-p admixture. Cd-d states are largely localized at deeper energies, yet their hybridization with anion p states can contribute to the p–d repulsion that shapes the valence edge. The bonding schematic in Fig. 3(d) provides an intuitive explanation for the aforementioned electronic structure features from a molecular orbital perspective. Ga-s–Te-p coupling forms a bonding manifold in the deep valence region and an antibonding counterpart that constitutes the conduction-band edge. The Cd–Te interaction, through p-d orbital hybridization, forms bonding states within the valence band and generates antibonding states near the Te-5p dominated VBM, which exhibit weak Cd-Te antibonding characteristics. The crystal orbital Hamilton population (COHP) [50] in Fig. 3(e) further supports the finding by revealing antibonding characters associated with Ga-Te near the CBM and Cd-Te near the VBM. The trend in anion evolution further validates this mechanism. As the electronegativity of the VI-site anion decreases with the cation fixed, the metal-anion bonds become longer, and the hybridization weakens, which reduces the bonding–antibonding splitting; together with the upward shift of the anion-p energy level for heavier chalcogens, this drives the VBM upward and tends to lower the antibonding CBM, resulting in an overall narrowing of E_g.

The reduction in band gap E_g typically lowers the energy threshold for electrons to be excited from the VBM to the CBM, leading to an increase in intrinsic carrier concentration and ultimately enhancing the electrical conductivity σ as shown in Fig. S15 of the SM. The microscopic origin of the variation in σ was further probed through a systematic analysis of the three dominant carrier-scattering mechanisms: acoustic deformation potential scattering (ADP), ionized impurity scattering (IMP), and polar optical phonon scattering (POP). These mechanisms directly determine σ by governing the carrier mobility μ ($\sigma = ne\mu$). The influence of scattering mechanisms on mobility follows a reciprocal relationship, i.e., carrier mobility is inversely proportional to the total scattering rate. Therefore, a low scattering rate of a scattering mechanism indicates weaker hindrance to carrier motion, which is conducive to achieving higher mobility. Figures 4(a) and 4(b) present the variations in mobility for mechanisms as functions of carrier concentration and scattering rates in $CdGa_2Te_4$ and $ZnGa_2S_4$, respectively. At 300 K and a carrier concentration of 10^{21} cm^{-3}, the scattering rate of ADP in both $CdGa_2Te_4$ and $ZnGa_2S_4$ is one order of magnitude lower than that of POP and IMP. Moreover, the scattering rates for mechanisms in $CdGa_2Te_4$ are slightly lower than those in $ZnGa_2S_4$. In both materials, the mobility dominated by ADP drops sharply when the carrier concentration exceeds 10^{19} cm^{-3}. Remarkably, the mobility of $CdGa_2Te_4$ is one order of magnitude higher than that of $ZnGa_2S_4$, indicating its significantly higher σ.

Figure 4(c) presents the carrier concentration dependence of σ, Seebeck coefficient S, electronic thermal conductivity κ_e, and power factor PF for $CdGa_2Te_4$ and $ZnGa_2S_4$. As discussed earlier, $CdGa_2Te_4$ exhibits significantly higher σ than $ZnGa_2S_4$. And this disparity becomes even more pronounced with increasing carrier concentration. In contrast to the upward trend of σ, the S of both materials gradually decreases as carrier concentration increases. $ZnGa_2S_4$ maintains a slightly higher S than $CdGa_2Te_4$ overall, which is closely related to their differences in band structure. As shown in Fig. S11 of the SM, $ZnGa_2S_4$ exhibits flatter band dispersion near the VBM, consistent with its larger hole effective masses along the Γ–N and Γ–M directions ($0.766m_0$ and $0.578m_0$) compared to those of $CdGa_2Te_4$ ($0.61m_0$ and $0.321m_0$). Since the S is positively correlated with carrier effective mass, $ZnGa_2S_4$ consequently exhibits relatively higher S values. Notably, although $ZnGa_2S_4$ exhibits a slightly larger S due to its heavier hole bands, $CdGa_2Te_4$ achieves a competitive S through valence-band degeneracy, while its lighter bands ensure higher σ. This enables a synergistic optimization of S and σ, resulting in an enhanced power factor. We also note the presence of conduction-band intervalley

degeneracy in $CdGa_2Te_4$ (Fig. S14 of the SM), though it does not directly affect the present p-type results. Based on the above electronic transport parameters, we further calculated the evolution of the *PF* with carrier concentration. Despite the coupling relationship between *S* and σ, $CdGa_2Te_4$ ultimately achieves a notable *PF* owing to its considerably higher σ. Additionally, the carrier concentration dependence of κ_e follows essentially the same trend as σ, which is expected due to the Wiedemann–Franz law ($\kappa_e = L\sigma T$, where *L* is the Lorenz number) [51]. It is worth emphasizing that when evaluating the total thermal conductivity of these materials, the contribution from κ_e cannot be neglected. The κ_e is comparable to or even higher than that of κ_L at elevated carrier concentrations.

Figures 4(d) and 4(e) present the evolution of *ZT* with carrier concentration for $CdGa_2Te_4$ and $ZnGa_2S_4$ at 300 K to evaluate the influence of 4ph scattering by comparing the results under two scenarios: one considering only 3ph scattering (ZT_{3ph}) and another incorporating both 3ph and 4ph scattering ($ZT_{3,4ph}$). Benefiting from an ultralow κ_L and a high *PF*, $CdGa_2Te_4$ exhibits promising thermoelectric potential at 300 K. Its ZT_{3ph} already reaches 0.270, being ten times larger than that of $ZnGa_2S_4$ (0.027). The inclusion of 4ph scattering enhances *ZT* for both materials, although the magnitude of the enhancement differs. $CdGa_2Te_4$ shows a dramatic rise in value from 0.290 to 0.689, corresponding to a ~2.4 times increase, whereas $ZnGa_2S_4$ exhibits only a modest increase from 0.027 to 0.048, marking a ~1.8 times enhancement. This reveals that 4ph scattering plays a decisive role in defective chalcopyrites. In addition, the *ZT* increases monotonically as the electronegativity of the VI-site anion decreases with the cation fixed. Such a trend aligns with the enhancement in σ shown in Fig. S15 of the SM.

Finally, we compared the *ZT* of $CdGa_2Te_4$ with those of several representative thermoelectric materials at 300 K. As illustrated in Fig. 4(f), $CdGa_2Te_4$ achieves a notable *ZT* of 0.689. This value drastically outperforms the other candidate materials such as the widely studied PbSe [52] and chalcopyrites (e.g., $AgSbTe_2$ [45] and $TlSbTe_2$ [46]), whose *ZT* values generally fall below 0.45 at 300 K. The significant performance improvement demonstrates that defective chalcopyrites with intrinsic vacancies, particularly $CdGa_2Te_4$, exhibit immense potential as high-performance thermoelectric materials. This promising performance is mainly attributed to the strong lattice anharmonicity caused by its unique ordered intrinsic vacancy structure. Such anharmonicity significantly enhances 4ph scattering and reduces κ_L to an ultra-low level. Meanwhile, the band structure ensures competitive electrical transport properties, enabling a favorable balance between thermal and electrical performance. Our findings not only reveal the critical role of vacancies in regulating lattice thermal transport properties but also provide a new strategy for exploring next-generation high-performance thermoelectric materials.

Conclusion

In summary, we have systematically elucidated the structure-property relationship governing thermoelectric performance in defective chalcopyrites. Ordered intrinsic vacancies are identified as the central structural motif responsible for their exceptional lattice thermal transport behavior. By further lowering crystal symmetry and amplifying local lattice distortion, vacancy ordering induces pronounced lattice anharmonicity, promotes MVB, and strengthens higher-order phonon interactions. Together with soft low-frequency phonons, strongly negative Grüneisen parameters, and reduced phonon group velocities, these effects make 4ph scattering a major heat-resistance mechanism and drive the lattice thermal conductivity to ultralow values. At the same time, the VI-site anion serves as an effective electronic approach: decreasing anion electronegativity elongates metal-anion bonds, weakens orbital hybridization, shifts anion p states upward, and narrows the band gap, thereby enhancing carrier transport. Owing to this synergistic optimization of phonon and electronic properties, $CdGa_2Te_4$ is identified as the optimal candidate in terms of overall thermoelectric performance, with a lattice thermal conductivity of 0.19 $W \cdot m^{-1} \cdot K^{-1}$ and a room-temperature *ZT* of 0.689. Beyond identifying this high-performance thermoelectric compound, this work integrates vacancy ordering and anion engineering as a unified design principle for developing next-generation thermoelectric materials based on defective chalcopyrite frameworks.

Data Availability

All data supporting this study's findings are available within the article. Additional data is available on request from the authors.

Acknowledgements

H.Z. and Y.L. acknowledge the National Key Research and Development Program of China (Grant No. 2023YFA1406200) and the Institute of High-pressure Physics of Ningbo University for its computational resources. J.Y. acknowledges the China Scholarship Council (Grant No. 202408330112). H.G. and Y.-W.F. acknowledge the financial support received from the IKUR Strategy under the collaboration agreement between Ikerbasque Foundation and Centro de Fśica de Materiales (CFM-MPC) on behalf of the Department of Science, Universities and Innovation of the Basque Government (HPCAI21: AI-CrysPred). Y.-W.F. is partially supported by the Extraordinary Grant of CSIC (Grant No. 2025ICT122) and acknowledge the support from the Spanish Ministry of Science and Innovation (Grant No. PID2025-173011NA-I00) funded by MICIU/AEI/10.13039/501100011033. W.R. gratefully acknowledges the computing time provided by the NHR Center NHR4CES at RWTH Aachen University under project p0027528, with funding from the German Federal Ministry of Research, Technology and Space and the German federal states through the National High-Performance Computing (NHR) joint funding program. S.L. acknowledges the computation resources provided by the National Academic Infrastructure for Supercomputing in Sweden (NAISS)—at supercomputer centers NSC and PDC, partially funded by the Swedish Research Council through grant agreement No. 2022-06725—and by the Vienna Scientific Cluster (VSC) in Austria.

References

[1] Su J, Liu Y, Li Y, Bai S, Gao D, Chen P, Zhao Z, Dravid V P, Xie H, Zhao L D, and Kanatzidis M G 2025 *J. Am. Chem. Soc.* **147** 16611
[2] Chen P, Xie H, and Zhao L D 2025 *Acta Metall. Sin.* **38** 707
[3] Kozai S, Suekuni K, Takahashi S, Nishibori E, Kasai H, Siloi I, Fornari M, Saito H, Sauerschnig P, Ohta M, Lemoine P, Guilmeau E, Raveau B, and Ohtaki M 2025 *J. Mater. Chem. A* **13** 10028
[4] Liang H P, Geng S, Jia T, Li C N, Xu X, Zhang X, and Wei S H 2024 *Phys. Rev. B* **109** 035205
[5] Lemoine P, Guélou G, Raveau B, and Guilmeau E 2022 *Angew. Chem. Int. Ed.* **61** e202108686
[6] Pang H, Bourges C, Jha R, Baba T, Sato N, Kawamoto N, Baba T, Tsujii N, and Mori T 2022 *Acta Mater.* **235** 118090
[7] Hu L, Luo Y, Fang Y W, Qin F, Cao X, Xie H, Liu J, Dong J, Sanson A, Giarola M, Tan X, Zheng Y, Suwardi A, Huang Y, Hippalgaonkar K, He J, Zhang W, Xu J, Yan Q, and Kanatzidis M G 2021 *Adv. Energy Mater.* **11** 2100661
[8] Li Z, Lee H, Wolverton C, and Xia Y 2026 *npj Comput. Mater.* **12** 51
[9] Xiong W, Xia Z, Han Z, Yao D, and He J 2026 *Phys. Rev. B* **113** 075204
[10] Guo S, Yue J, Zheng J, Zhang H, Wang N, Li J, Liu Y, and Cui T 2025 *Phys. Rev. B* **111** 184312
[11] Huang L, Li Y, Sha S, Ge B, Wu Y, Yan J, Kong Y, and Zhang J 2023 *Small* **19** 2206865
[12] Cao Y, Su X, Meng F, Bailey T P, Zhao J, Xie H, He J, Uher C, and Tang X 2020 *Adv. Funct. Mater.* **30** 2005861
[13] Zhang J, Huang L, Zhu C, Zhou C, Jabar B, Li J, Zhu X, Wang L, Song C, Xin H, Li D, and Qin X 2019 *Adv. Mater.* **31** 1905210
[14] Li Y, Liu J, and Hong J 2022 *Phys. Rev. B* **106** 094317
[15] Zheng J, Shi D, Yang Y, Lin C, Huang H, Guo R, and Huang B 2022 *Phys. Rev. B* **105** 224303
[16] Yue J, Guo S, Li J, Zhao J, Shen C, Zhang H, Liu Y, and Cui T 2023

Mater. Today Phys. **39** 101283
[17] Zheng J, Chang Z, Lin C, Lin C, Zhou Y, Huang B, Guo R, and Hautier G 2025 *npj Comput. Mater.* **11** 315
[18] Wei J, Yu W, Li Z, Hu J, Wang T, Yu Y, and Guo X 2025 *Chem. Eng. J.* **521** 166531
[19] Miglio A, Heinrich C P, Tremel W, Hautier G, and Zeier W G 2017 *Adv. Sci.* **4** 1700080
[20] Xu T, Bai W, Qin M, Huang L, Liu Y, Wang S, Li Z, Yuan Z, Xin H, Li D, Huang Z, Chen P, Liu X, Zhang Y, Xiao C, Zhang J, and Xie Y 2026 *J. Am. Chem. Soc.* **148** 12343
[21] Xiong Q, Wu H, Zhang K *et al* 2024 *Acta Mater.* **278** 120268
[22] Zhang Q, Gu B, Wu Y, Zhu T, Fang T, Yang Y, Liu J, Ye B, and Zhao X 2019 *ACS Appl. Mater. Interfaces* **11** 41424
[23] Zheng X, Li A, Liu S, Han Z, Zhang M, Liu F, Fu C, and Zhu T 2023 *Acta Mater.* **260** 119346
[24] Tan S, Jiang L, Kang H, Chen R, Chen Z, Guo E, and Wang T 2026 *Small* **22** e13437
[25] Xie H, Bozin E S, Li Z, Abeykoon M, Banerjee S, Male J P, Snyder G J, Wolverton C, Billinge S J, and Kanatzidis M G 2022 *Adv. Mater.* **34** 2202255
[26] Caro-Campos I, Posligua V, Prado-Gonjal J, Dura O J, Nemes N M, Gainza J, Martínez J L, Alonso J A, Márquez A M, Plata J J, and Serrano-Sanchez F 2026 *Small Struct.* **7** e202500800
[27] Knoop F, Purcell T A, Scheffler M, and Carbogno C 2023 *Phys. Rev. Lett.* **130** 236301
[28] Raty J Y, Schumacher M, Golub P, Deringer V L, Gatti C, and Wuttig M 2019 *Adv. Mater.* **31** 1806280
[29] Cheng L, Li M, Zhang L, and Wang H 2025 *Phys. Rev. B* **112** 045202
[30] Govindaraj P, Murugan K, Veluswamy P, and Venugopal K 2023 *J. Solid State Chem.* **324** 124076
[31] Saal J E, Kirklin S, Aykol M, Meredig B, and Wolverton C 2013 *JOM* **65** 1501
[32] Yu H, Chen L C, Pang H J, Qiu P F, Peng Q, and Chen X J 2022 *Phys. Rev. B* **105** 245204
[33] Suriwong T, Kurosaki K, and Thongtem 2011 *J. Alloys Compd.* **509** 7484
[34] Knoop F, Purcell T A, Scheffler M, and Carbogno C 2020 *Phys. Rev. Mater.* **4** 083809
[35] Petley B W 2002 *IEEE Trans. Instrum. Meas.* **38** 175
[36] Yu Y, Cagnoni M, Cojocaru-Mirédin O, and Wuttig M 2020 *Adv. Funct. Mater.* **30** 1904862
[37] Yue J, Liu Y, Ren W, Lin S, Shen C, Singh H K, Cui T, Tadano T, and Zhang H 2024 *Mater. Today Phys.* **41** 101340
[38] Yuan K, Zhang X, Gao Y, and Tang D 2023 *Phys. Chem. Chem. Phys.* **25** 24883
[39] Han Z, Yang X, Li W, Feng T, and Ruan X 2022 *Comput. Phys. Commun.* **270** 108179
[40] Yue J, Zheng J, Li J, Guo S, Ren W, Liu H, Liu Y, and Cui T 2024 *ACS Appl. Mater. Interfaces* **16** 20597
[41] Yue J, Zheng J, Shen X, Maji K, Yang C C, Lin S, Lemoine P, Guilmeau E, Liu Y, and Cui T 2025 *Small* **21** e06386
[42] Zheng J, Lin C, Lin C, Hautier G, Guo R, and Huang B 2024 *npj Comput. Mater.* **10** 30
[43] Chen Z G, Shi X, Zhao L D, and Zou J 2018 *Prog. Mater. Sci.* **97** 283
[44] Liang J, Wang T, Qiu P, Yang S, Ming C, Chen H, Song Q, Zhao K, Wei T R, Ren D, Sun Y Y, Shi X, He J, and Chen L 2019 *Energy Environ. Sci.* **12** 2983
[45] Li N H, Zhang Q, Shi X L, Jiang J, and Chen Z G 2024 *Adv. Mater.* **36** 2313146
[46] Wang H, Charoenphakdee A, Kurosaki K, Yamanaka S, and Snyder G J 2011 *Phys. Rev. B* **83** 024303
[47] Shi H, Wen Y, Bai S *et al* 2025 *Nat. Commun.* **16** 1788
[48] Liu H M, Wu X Q, Sun J Y, Li S, Zhang J X, Ye X L, and Zhang Q 2025 *Rare Met.* **44** 1213
[49] Zhao P, Xue W, Zhang Y *et al* 2024 *Nature* **631** 777
[50] Dronskowski R and Bloechl P E 1993 *J. Phys. Chem.* **97** 8617
[51] Chester G and Thellung A 1961 *Proc. Phys. Soc.* **77** 1005
[52] Liu S, Qin Y, Wen Y, Shi H, Qin B, Hong T, Gao X, Cao Q, Chang C, and Zhao L D 2024 *Adv. Funct. Mater.* **34** 2315707